Research Square

Preprints are preliminary reports that have not undergone peer review.
They should not be considered conclusive, used to inform clinical practice,
or referenced by the media as validated information.

Wearable 16-channel electroencephalography for 8-day continuous monitoring

Zongman Zhang
Guangdong Technion – Israel Institute of Technology
Yi Liu
Guangdong Technion – Israel Institute of Technology
Wenqing Yan
Guangdong Technion – Israel Institute of Technology
Haoyang Wang
The University of Tokyo
Shihong Lin
Guangdong Technion – Israel Institute of Technology
Jiawei Yang
Guangdong Technion – Israel Institute of Technology
Zonglei Wang
Guangdong Technion – Israel Institute of Technology
Yuli Wang
Guangdong Technion – Israel Institute of Technology
Jiansheng Zhang
Shantou University
Yumiao Xu
Guangdong Technion – Israel Institute of Technology
Pengcheng Zhou
Guangdong Technion – Israel Institute of Technology
Yujie Zhang
Guangdong Technion – Israel Institute of Technology
Mingzhe Wang
Guangdong Technion – Israel Institute of Technology
Zichong Ji
Guangdong Technion – Israel Institute of Technology
Meiqiong Zheng
Guangdong Technion – Israel Institute of Technology
Shuaizhe Chen
Guangdong Technion – Israel Institute of Technology
Yun Li

Shantou University

Tomoyuki Yokota

The University of Tokyo https://orcid.org/0000-0003-1546-8864

Sunghoon Lee

The University of Tokyo https://orcid.org/0000-0002-3592-388X

Takao Someya

someya@g.ecc.u-tokyo.ac.jp

The University of Tokyo https://orcid.org/0000-0003-3051-1138

Yan Wang

wang.yan@technion.ac.il

Guangdong Technion – Israel Institute of Technology https://orcid.org/0000-0002-5224-0941

Research Article

Keywords: epidermal electronics, wireless electroencephalography, long-term health monitoring, daily monitoring

Posted Date: June 10th, 2026

DOI: https://doi.org/10.21203/rs.3.rs-9983631/v1

License: This work is licensed under a Creative Commons Attribution 4.0 International License. Read Full License

Additional Declarations: The authors declare no competing interests.

Wearable 16-channel electroencephalography for 8-day continuous monitoring

Authors: Zongman Zhang[1,2†], Yi Liu[1,2†], Wenqing Yan[1,2†], Haoyang Wang[3,4†], Shihong Lin[1,2], Jiawei Yang[1,2], Zonglei Wang[1,2], Yuli Wang[1,2], Jiansheng Zhang[5,6], Yumiao Xu[1], Pengcheng Zhou[1,2], Yujie Zhang[1,2], Mingzhe Wang[1], Zichong Ji[1,2], Meiqiong Zheng[1,2], Shuaizhe Chen[7], Yun Li[5,6], Tomoyuki Yokota[3], Sunghoon Lee[3,8], Takao Someya[3,8*] and Yan Wang[1,2,9*]

Affiliations:

[1] Department of Chemical Engineering, Guangdong Technion – Israel Institute of Technology, 241 Daxue Road, Shantou, Guangdong 515063, China

[2] Department of Chemical Engineering, Technion – Israel Institute of Technology, Haifa 3200003, Israel

[3] Department of Electrical Engineering and Information Systems, The University of Tokyo, 7-3-1, Bunkyo-ku, Tokyo 113-8656, Japan

[4] School of Electronic Science & Engineering, Southeast University, 2 Southeast University Road, Nanjing, Jiangsu 211189, China

[5] Department of Sleep Medicine, Mental Health Center of Shantou University, Shantou, Guangdong, China

[6] Shantou University Medical College-Faculty of Medicine of University of Manitoba Joint Laboratory of Biological Psychiatry, Shantou, Guangdong, China

[7] Department of Materials Science and Engineering, Guangdong Technion – Israel Institute of Technology, 241 Daxue Road, Shantou, Guangdong 515063, China

[8] RIKEN Center for Emergent Matter Science, 2-1 Hirosawa, Wako, Saitama, 351-0198, Japan

[9] Guangdong Provincial Key Laboratory of Materials and Technologies for Energy Conversion, Guangdong Technion – Israel Institute of Technology, 241 Daxue Road, Shantou, Guangdong 515063, China

[†]These authors contributed equally to this work.

*Correspondence to: someya@ee.t.u-tokyo.ac.jp; wang.yan@technion.ac.il

Abstract: Monitoring cognitive state in everyday life requires unobtrusive electroencephalography (EEG), yet conventional systems rely on non-breathable contacts that dry and slip on hair and on bulky, low-channel hardware that compromises comfort and signal fidelity. We introduce a fully breathable, integrated wearable EEG system that enables week-scale daily brain recording with smartphone-based attention assessment. An in situ-gelled, macroporous hydrogel coupled to a thin, flexible Ag/AgCl mesh electrode establishes a hair-compatible, anti-drying, friction-resistant scalp–hydrogel–electrode interface that maintains stable long-term signals. An earhook wireless module with macroporous silicone encapsulation enhances breathability and comfort, while a wirelessly rechargeable battery supports continuous operation

in everyday settings. During treadmill running (6.5 km h^{-1}), the hydrogel interface suppresses stride-locked artefacts (3.02 Hz) and increases signal-to-noise ratio relative to commercial EEG paste electrodes. Overnight wireless recordings yield sleep staging and spectral metrics comparable to polysomnography benchmarking. Extending on these validations, we demonstrate continuous 16-channel scalp EEG over 8 days of naturalistic activity and use machine-learning algorithms to generate real-time attention assessment via a smartphone interface. This breathable, durable architecture enables unobtrusive, longitudinal neurophysiology and opens avenues for neurological disease monitoring, learning and performance support, workplace safety, and ecologically valid brain research.

Introduction

Non-invasive high-precision EEG monitoring of microvolt-level neural signals underpins advances in cognitive-state tracking[1,2], neurodegenerative disease management[3,4], brain-machine interfaces (BMIs)[5,6]. Conventional, high-density systems excel in controlled environments[7,8], but there is strong interest in wearable platforms that enhance comfort and mobility to enable ambulatory monitoring[9-11]. Notable progress includes fully portable, wireless 2-channel scalp systems that pair flexible electronics with deep learning for universal BMIs[12] and in-ear integrated sensor arrays for unobtrusive brain-state monitoring within the ear canal[13]. Building on these developments, achieving high-quality, high-spatial-resolution EEG over extended periods in everyday settings remains an active area of research[14]. In particular, carefully balancing form factor, breathability, skin–electrode interface stability, channel number, and energy capacity is essential for stable long-duration, wireless recordings **(Supplementary Table 1)**.

The skin–electrode interface is central to these goals. Scalp electrodes generally offer higher spatial fidelity than periauricular or forehead placements owing to coverage and proximity[15,16]. Across electrode classes, dry, semi-dry, and wet, each approach entails characteristic trade-offs **(Supplementary Table 2)**. Dry electrodes, including flexible metal-coated bristles and conductive polymers, can establish hair-through contact and may use external pressure or tailored mechanics to ensure consistent coupling; planar variants typically require hair shaving[17,18]. Semi-dry designs employ sponges or electrolytic reservoirs with periodic replenishment[19,20]. Wet electrodes use conductive gels, pastes, or inks to navigate hair and often benefit from cap-based stabilization over continuous recording sessions[21,22]. Hydrogels have emerged as promising interfaces due to their softness, conductivity, and adhesion[23,24]. For continuous daily use, strategies that enhance breathability, friction tolerance under hair, mechanical robustness, and anti-drying property are pivotal for high-quality signal acquisition[25-27]. As summarized in **Supplementary Table 3**, there remains a gap for breathable, durable hair-bearing scalp–hydrogel–electrode interfaces enabling high-quality signals in everyday use.

Here, we introduce a fully breathable, integrated wearable EEG system that addresses these needs through a macroporous, in situ-gelled hydrogel integrated with a flexible Ag/AgCl mesh electrode, forming a hair-compatible, anti-drying, friction-resistant scalp–hydrogel–electrode interface that maintains high-quality signals during daily activities. An earhook wireless module with macroporous silicone elastomer (Ecoflex) encapsulation and an embedded wirelessly rechargeable battery supports continuous daily operation. The system maintains high signal quality during running with minimal motion artefacts, captures sleep metrics comparable to polysomnography (PSG), and enables continuous 16-channel recordings over 8 days during naturalistic activities. Smartphone-based analytics provide real-time attention estimates for on-device cognitive state monitoring.

Results

System design and 8-day continuous daily monitoring

The system integrates an in situ-gelled, macroporous hydrogel with a thin, flexible Ag/AgCl mesh electrode and an ergonomically designed 16-channel earhook wireless module **(Fig. 1a and Supplementary Fig. 1)**. Breathability arises from the combination of the macroporous hydrogel interface, the Ag/AgCl mesh architecture, and a macroporous Ecoflex encapsulation for the wireless module **(Fig. 1a, i and iii and Supplementary Figs. 1a and 2)**. **Fig. 1a, ii–iii and Supplementary Fig. 1b** illustrate the mechanical flexibility of the earhook module and the mesh electrode, respectively. The ultrathin Ag/AgCl mesh was chosen to combine mechanical compliance with electrochemical stability, reducing interfacial polarization and potential drift for low-noise EEG acquisition[28]. The open-mesh architecture of the Ag/AgCl electrode also enables hydrogel infiltration. After the hydrogel precursor is painted onto the skin, it penetrates the mesh apertures during cooling-induced gelation and embeds the electrode within the macroporous matrix, creating a three-dimensionally interlocked skin/substrate–hydrogel–electrode–hydrogel interface with strong mechanical anchoring and reduced interfacial perturbation from relative slippage **(Supplementary Fig. 1c)**. Together with the hydrogel's inherent adhesiveness and in situ gelation, this design enables robust coupling to both hair-bearing scalp and smooth skin, thereby maintaining a stable bioelectronic interface **(Fig. 1a, i, Supplementary Fig. 3 and Supplementary Video 1)**.

The earhook module houses low-noise 16-channel EEG acquisition, amplification, and digitization, power regulation, Bluetooth low energy (BLE) telemetry, a remote reception unit, and an inductive charging coil **(Methods and Supplementary Fig. 1d)**. It connects to the Ag/AgCl mesh electrodes via thin, flexible commercial wires **(Fig. 1a, iii and Supplementary Figs. 1a,b)**. Hereafter, we use "hydrogel" for the macroporous hydrogel and "hydrogel electrode" for that hydrogel integrated with a flexible Ag/AgCl mesh electrode.

A topologically optimized 16-channel montage provides broad scalp coverage over frontal (F_3, F_Z, F_4), central (C_3, C_Z, C_4), parietal (P_3, P_Z, P_4, P_7, P_8), occipital (O_1, O_Z, O_2), and temporal (T_7, T_8) sites (10–20 international electrode placement system)[29]. This arrangement provides broad sensor-level coverage of scalp activity linked to distributed attention-related cortical systems, particularly frontal control and parietal orienting networks, as well as their associated large-scale dynamics **(Fig. 1b, i)**[30,31]. On-device analysis converts the 16-channel EEG into time-frequency features using the short-time Fourier transform (STFT), and an embedded machine-learning algorithm estimates the attention level in real-time **(Fig. 1b, ii)**. The smartphone interface displays a scalar attention level, a dynamic attention trace, and 16-channel EEG signals.

In everyday settings, the fully breathable wearable system achieved up to 8 days of unobtrusive brain-activity monitoring with real-time attention assessment, spanning ambulatory and sedentary behaviors, including walking (~2 km h^{-1}), casual smartphone use at a bus stop, deskwork, and sleep **(Fig. 1c, i–iv)**. Scalp topographies of θ (4–8 Hz)-, α (8–12 Hz)-, and β (12–30 Hz)-band power are shown for representative tasks **(Supplementary Fig. 1e, top and Fig. 1c, insets)**. The smartphone screenshot illustrates distinct attention levels for walking, casual smartphone use while waiting, deskwork, and sleep (scores: 7, 33, 84, and 0, respectively) **(Supplementary Fig. 1e, bottom)**. During walking, hydrogel electrodes provided a higher signal-to-noise ratio (SNR; 18.7 dB) than commercial EEG paste (8.5 dB), indicating improved robustness to motion-induced artefacts **(Fig. 1c, inset i)**. Inductive charging during sleep enables uninterrupted overnight

operation **(Fig. 1c, inset iv)**.

Hydrogel characterization

We engineered permeable scalp–hydrogel interface via a thermally regulated sol−gel transition with a phase transition temperature of 39 °C **(Fig. 2a and Supplementary Fig. 4)**. Fabrication proceeds by (i) generating air bubbles in a viscous precursor by vortex stirring at ~75 °C, (ii) painting the resulting gaseous dispersion onto the hair-bearing scalp at ~40 °C, and (iii) locking the pores by cooling-induced gelation at scalp temperature (~ 34 °C) **(Fig. 2a)**.

The hydrogel comprises gelatin as a three-dimensional scaffold, a water–glycerol binary solvent to suppress dehydration (water-locking), dopamine hydrochloride (DA·HCl) to promote catechol-mediated bio-adhesion, and tannic acid (TA) as a dynamic crosslinker and adhesion promoter via phenolic-hydroxyl hydrogen bonding. Systematic evaluations of hydrogel–skin contact impedance, adhesion, stretchability, gelation time, anti-drying performance, and intrinsic impedance identified an optimal composition **(**see **Methods, Supplementary Note 1, Supplementary Figs. 5–9 and Supplementary Table 4)**. The prepared hydrogel also exhibits pronounced self-healing performance **(Supplementary Fig. 10)**.

Stirring rate governed precursor viscosity, which needed to be high enough to prevent bubble coalescence, rupture and collapse before gelation, yet low enough to allow bubble generation during stirring. By controlling precursor viscosity, stirring rate also determined pore structure and, consequently, permeability **(Supplementary Note 2 and Supplementary Fig. 11)**. Among hydrogels prepared at 500, 1,000 and 1,500 rpm, the sample prepared at 1,000 rpm exhibited a viscosity of 1.9 ± 0.2 Pa s and formed a macroporous network with a pore size of 304.6 ± 81.3 μm, together with the highest air permeance and a high water-vapor transmission rate (WVTR) **(Figs. 2b,c and Supplementary Fig. 12)**. Cross-sectional scanning electron microscopy (SEM) clearly distinguished hydrogels formed at different stirring speeds from the non-porous control **(Supplementary Fig. 13)**.

We next quantified permeability by comparing gas and water-vapor transport across the hydrogel, hydrogel electrode, non-porous hydrogel and parylene **(Fig. 2d)**. The hydrogel showed an air permeance of $22{,}956.4 \pm 1{,}587.5$ in gas permeance units (GPU; 1 GPU = 10^{-6} cm^3 (STP) cm^{-2} s^{-1} $cmHg^{-1}$), approximately 272-fold that of a composition-matched, non-porous counterpart. **Supplementary Video 2** qualitatively illustrates rapid air permeation in both water and soapy water. We attribute this enhancement to shortened transport pathways within the interconnected macroporous network. Consistent with this mechanism, the hydrogel also showed a higher WVTR than the non-porous hydrogel, whereas dense parylene imposed severe diffusional constraints **(Supplementary Note 3 and Supplementary Fig. 14)**. The hydrogel electrodes likewise exhibited gas and water-vapor permeabilities comparable to those of the hydrogel.

In situ gelation allowed the hydrogel to infiltrate dense hair and conform to irregular scalp microtopography, whereas preformed gels could not achieve such intimate contact **(Supplementary Fig. 15, left)**. From 90° peel tests, interfacial toughness reached $4{,}958.1 \pm 483.6$ J m^{-2} for hair-bearing skin–hydrogel and $1{,}485.1 \pm 204.3$ J m^{-2} for smooth skin–hydrogel, representing 601- and 24-fold improvements over pre-formed, non-infiltrating controls **(Supplementary Fig. 15, right)**. Adhesion arises from cooperative hydrogen bonding and electrostatic interactions with the stratum corneum, while hair shafts provide additional mechanical interlocking **(Supplementary Fig. 16)**. FTIR analysis supports these assignments **(Supplementary Fig. 17)**. The hydrogel–electrode interface exhibited an interfacial adhesive

force of 30.9 N cm^{-1}, substantially exceeding that of commercial EEG paste **(Supplementary Figs. 18 and 19)**.

Mechanical and electrical robustness were validated under friction and compression. A micro-LED remained stably illuminated on the hair-bearing scalp during repetitive rubbing with a friction ball for 1 h **(Fig. 2e, left)**. Quantitatively, the hydrogel retained its electrical functionality over 1,000 friction cycles, whereas the commercial EEG paste lost conductivity after 50 friction cycles **(Fig. 2e, right)**. After 24 h under a 500 g compressive load, the hydrogel maintained macroporosity, thickness, and pore morphology **(Fig. 2f and Supplementary Fig. 20)** and showed high durability under repeated compression and stretching **(Supplementary Figs. 21 and 22)**.

During 8 days of continuous wear, interfacial toughness declined slightly yet remained high: 958.3 ± 62.9 J m^{-2} (hair-bearing skin–hydrogel) and 3,622.1 ± 343.2 J m^{-2} (hydrogel–electrode) by Day 8 **(Fig. 2g)**. The non-toxic, biocompatible components, together with high breathability, supported physiological comfort and skin health; no adverse sensations or inflammation were reported **(Fig. 2h and Methods)**.

The hair-bearing scalp–hydrogel achieved an initial contact impedance of 10.4 kΩ cm^2 at 0.1 Hz (remaining 17.0 kΩ cm^2 after 24 h), outperforming commercial EEG paste (19.7 kΩ·cm^2 initially), which failed due to detachment after ~9 h wear **(Supplementary Fig. 23)**. Over the 8-day continuous wear, 16-channel scalp contact impedances rose gradually due to sebum accumulation and hair growth **(**0.5–1.7 cm $month^{-1}$; **Fig. 2i)**, reaching an average of 380.1 kΩ cm^2, which remained sufficient for high-quality EEG monitoring[33]. Brief warm-air exposure (hair dryer) restored the conformal interface, reducing impedance to 61.7 kΩ cm^2 (16-channel average) at 10 Hz **(Supplementary Fig. 24)**. Finally, leveraging the reversible thermal phase change, the hydrogel can be remolded into diverse geometries and reused without measurable performance degradation **(Supplementary Figs. 25 and 26)**, and it can be removed readily by warm water rinsing after use **(Supplementary Fig. 27)**.

PSG benchmarking and motion artefact evaluation

We conducted PSG validation at a sleep medicine department by benchmarking the wireless system against a hospital PSG platform **(**see **Methods and Supplementary Video 3)**. As shown in **Fig. 3a**, the wireless setup offers high wearability and comfort. For side-by-side comparison, hydrogel electrodes were placed at F_3, F_4, C_3, C_4, O_1, and O_2 (10–20 system), with commercial EEG paste electrodes positioned at adjacent sites. Simultaneous PSG and wireless recordings were acquired for 8.5 h. Representative EEG signals show closely matched waveforms **(Supplementary Fig. 28)**, and a sleep technician scored with blind datasets according to American Academy of Sleep Medicine (AASM) criteria[32].

STFT-based time-frequency analysis revealed highly consistent spectral structure across systems **(Fig. 3b)**. Zoom-in EEG traces across sleep stages revealed characteristic sleep graphoelements, including N2 spindles and K-complexes and N3 slow waves, with stage-specific cross-system Pearson correlation coefficients > 0.81 **(Fig. 3c)**. Minor discrepancies are attributable to the intentional electrode offset (~1.5 cm) and differing sampling rates (512 Hz for PSG; 250 Hz for wireless). Hypnograms and the confusion matrix demonstrated strong agreement over the full night (97.06% overall; Cohen's Kappa coefficient (κ) = 0.96), indicating near-perfect inter-system concordance **(Figs. 3d,e)**.

Because motion artefact suppression is critical for daily use, we integrated a triaxial accelerometer

and quantified artefacts at T_8, P_4, and F_4 channels during slow walking (2.0 km h^{-1}), fast walking (5.0 km h^{-1}), and running (6.5 km h^{-1}) **(**see **Methods)**. **Figures 3f–h** summarize T_8 results: (i) measurement photographs, (ii) representative EEG signals and SNR results, (iii) fast Fourier transform (FFT) amplitude spectra of vertical-axis acceleration (Az) and EEG, and (iv) wavelet coherence between Az and EEG. Across all speeds, the commercial EEG paste electrodes exhibited higher motion-induced noise than the hydrogel electrodes. At 2.0 km h^{-1}, SNRs were 8.5 dB (commercial EEG paste) versus 18.7 dB (hydrogel), confirming robust low-gait speed acquisition **(Fig. 3f, ii)**. With increasing speed, both electrodes showed larger fluctuations and declining SNR, yet the hydrogel consistently outperformed commercial EEG paste **(Fig. 3g,h, ii)**. FFT preserved the characteristic 1/f EEG spectrum; at slow walking (0.93 Hz step frequency), neither recording showed a pronounced gait-frequency peak, consistent with weaker gait coupling **(Fig. 3f, iii)**. At higher step frequencies (2.32 Hz and 3.02 Hz), gait-locked peaks and harmonics emerged, markedly stronger for commercial EEG paste than for hydrogel, indicating superior hydrogel suppression of periodic motion contamination **(Fig. 3g,h, iii)**. Wavelet coherence corroborated these trends: commercial EEG paste electrodes exhibited strong Az–EEG coherence (> 0.75) at step frequencies, whereas hydrogel electrodes maintained substantially lower coherence **(Fig. 3f–h, iv)**. Channel-matched analyses for P_4 and F_4 yielded consistent results **(Supplementary Figs. 29 and 30)**. After 45 min of high-intensity exercise, hydrogel electrodes still delivered high SNR walking data at 2.0 km h^{-1} **(Supplementary Fig. 31)**. Extending to 24 h continuous monitoring, commercial EEG paste electrodes progressively degraded and detached after ~11 h, while hydrogel electrodes preserved adhesion, structural integrity, and signal quality throughout, even during 4 walking workouts (5.0 km h^{-1}) **(Supplementary Note 4 and Supplementary Fig. 32)**.

On-device attention assessment

We then used the wireless system to contrast activities with distinct attention demands: a high-attention Schulte Grid "number-search" task and a low-attention relaxing state. 16-channel EEG signals dissociated the conditions, showing faster rhythms during number-search and slower waves during relaxing **(Supplementary Fig. 33)**. **Figure 4a** shows representative measurement scenes, scalp topographies of θ-, α-, and β-band power, 16-channel averaged power spectral density (PSD), and 16-channel functional connectivity networks for the low-attention relaxing state and the high-attention number-search condition **(**data processing see **Methods)**.

During relaxation, the PSD displayed a pronounced α-band peak, with elevated low-frequency power and relatively sparse functional connectivity, consistent with default-mode network engagement and reduced attentional load[33]. In contrast, the number-search task elicited robust α-related desynchronization, task-related reorganization of θ activity, and enhanced β-band power. The corresponding functional connectivity map exhibited stronger and more spatially distributed long-range connections across frontal, central, parietal, and temporal regions, reflecting increased large-scale coordination during task performance[34-36]. The engagement index, $\beta/(\alpha + \theta)$, was significantly higher during the number-search task than during relaxation **(Supplementary Fig. 34)**, confirming greater attentional engagement[37,38].

Building on these discriminative features between relaxed and cognitively engaged states, we implemented a smartphone-based, real-time attention-scoring model **(Fig. 4b)**. The 16-channel EEG signals were processed online using STFT with 2 s windows with 50% overlap. Spectral features within the 4–30 Hz band were extracted and assembled into 20 s analysis segments, with consecutive segments generated every 1 s. Within each segment, channel-wise spectral features

were reshaped into a two-dimensional feature matrix and fed into a recurrent regression model consisting of three stacked long short-term memory (LSTM) layers, followed by a fully connected layer and a Hardtanh activation function constrained to the range 0–1. The resulting values were linearly transformed to a 0–100 scale to generate an attention score with 1 s temporal resolution **(**see **Methods)**.

Across 4 alternating relaxing–number-search–relaxing blocks, the model recapitulated task structure with periodic increases during number-search and decreases during relaxing **(Fig. 4c)**. Cross-participant evaluation (n = 6) showed close agreement between model outputs and participants' Likert-scale self-ratings **(Supplementary Table 5)** during focused cognitive activity number-search, distracted number-search induced by conversation with another person, and relaxing periods **(Fig. 4d)**. In a driving simulation for participant E, the system distinguished attention states across focused driving, relaxing, post-rest focused driving, and phone-call-induced dual-task distraction **(Fig. 4e)**. Attention scores rose during sustained focused driving, declined during relaxing, and recovered when driving resumed; under phone-call distraction, the model captured pronounced fluctuations with an overall downward trend, indicating sensitivity to sustained cognitive load and real-world distractions **(Supplementary Video 4)**.

Eight-day continuous daily recording

Eight-day continuous monitoring was conducted in naturalistic settings. A participant wore the wireless system throughout daily activities, including walking, meeting, deskwork, casual chatting, exercise, and sleep. To facilitate behavioral annotation, daily routines were segmented into 18 activities and consolidated into five color-coded categories: exercise (red), recreational activity (blue), cognitively demanding activity (yellow), restful state (gray), and other daily routines (green), for analysis **(Fig. 5a and Supplementary Fig. 35)**.

The complete 8-day recording shows 16-channel EEG signals alongside per-second attention scores **(Fig. 5a)**. The attention trajectories show a stable diurnal rhythm that parallels the multiscale patterns observed in the time-frequency spectrograms **(Supplementary Fig. 35a)**. Ridgeline distributions further reveal activity-dependent attention profiles spanning dynamic behaviors (e.g., stretching, cycling, rowing, walking), static behaviors (e.g., sleep, deskwork, meditation), and other daily routines (e.g., housework and showering) **(Fig. 5b, Supplementary Fig. 35b and Supplementary Video 5)**. Mean attention levels in **Fig. 5b and Supplementary Fig. 35b** track the cognitive load associated with each labeled activity.

Deskwork shows a bimodal distribution of attention levels, with two peaks at 23.21 and 64.47 **(Fig. 5b, yellow ridgeline)**, indicating pronounced fluctuations in cognitive engagement during this activity across the 8-day period. To further examine within-task variability, 3 representative 5-min deskwork epochs were extracted from Days 1, 4, and 7 **(Fig. 5c)**. Attention varied periodically (e.g., Day 1: ~85 versus ~19; Day 4: ~89 versus ~17; Day 7: ~80 versus ~15), reflecting natural state transitions under sustained cognitive load and demonstrating the system's ability to capture moment-to-moment attentional dynamics.

Scalp topographies of θ-, α-, and β-band power at selected time points (i–vi) reveal reproducible contrasts between high- and low-attention states **(Fig. 5c, insets)**. During high-attention periods, the observed pattern is characterized by relatively elevated β-band power, reduced θ activity, and attenuated α power outside the occipital region, consistent with sustained task engagement. During low-attention periods, θ power increases, α power rebounds over parieto-occipital regions, and β activity decreases, a pattern broadly consistent with reduced attentional control and mind-

wandering, although such spectral markers are known to be task- and context-dependent. θ oscillations are commonly linked to cognitive control and memory-related processing, α oscillations to attentional selection and suppression, and β oscillations to maintenance of the current cognitive state[39-41].

Quantification using the engagement index $\beta/(\alpha + \theta)$ clearly separated high- and low-attention states across all 3 deskwork sessions, with high-attention values approximately 2- to 3-fold higher than low-attention values (i versus ii on Day 1, iii versus iv on Day 4, and v versus vi on Day 7) **(Fig. 5d)**. Day-to-day reproducibility of the separation between high- and low-attention states within the same labeled activity demonstrates that the system can reliably and stably capture moment-to-moment fluctuations in cognitive state over 8 days of continuous monitoring.

Across 8 sleep sessions, both the mode and mean of attention remained low (mode = 2.58), consistent with typical sleep neurophysiology **(Fig. 5e)**. Long-duration operation was further supported by wireless charging during sleep, which prevented power interruptions **(Supplementary Video 6)**.

We next examined within- and across-day paradigms encompassing both rapid cognitive state switches and repeated behaviors in natural contexts, including alternating cognitive activity/rest tasks (number-search–relaxing–number-search; number-write–relaxing–number-write), diverse exercise routines, various relaxation conditions, and repeated executions of identical tasks at different times **(Supplementary Note 5 and Supplementary Figs. 36–43)**. Across 8 consecutive days, the real-time attention readout consistently separated closely related, repeatedly occurring activity patterns, indicating both high task discriminability and longitudinal stability suitable for extended behavioral monitoring.

Supplementary Fig. 41 provided a test in verbal communication contexts. Continuous EEG and attention trajectories on Day 6 exhibited minute-to-hour fluctuations that aligned closely with annotated activities, showing abrupt transitions at task boundaries and sustained plateaus during extended conversations **(Supplementary Fig. 41a)**. Activity-stratified ridgeline plots revealed separable attention distributions across categories **(Supplementary Fig. 41b)**: verbal tasks (meeting, research discussion, and casual chatting) were right-shifted relative to deskwork, whereas passive digital media and casual smartphone use occupied lower ranges; sleep formed a floor distribution. Representative 10 s EEG segments illustrated distinct spectral content across conversation types **(Supplementary Fig. 41c)**. **Supplementary Fig. 41d** shows a graded pattern across the selected exemplars with attention highest of 82 during the meeting segment, intermediate of 51 during the research discussion segment, and lowest of 13 during the casual chatting segment. The corresponding θ-, α-, and β-band topographies qualitatively suggest lower α power and relatively higher β power in the high-attention state than in the low-attention state, with the intermediate state showing a transitional pattern **(Supplementary Fig. 41d, insets)**. These patterns are broadly consistent with prior studies showing that EEG modulation during social interaction is task-dependent, with verbal turn-taking linked to temporal–parietal theta/alpha activity and interactive contexts showing stronger alpha/low-beta modulation[42,43]. This yielded a graded engagement profile, with the engagement index highest during meetings, intermediate during research discussions, and lowest during casual chatting **(Supplementary Fig. 41e)**.

Data quality remained consistently high throughout 8 days. The only major interruption was ~10 h of inadvertent F_3 disconnection during sleep on Day 3, which resolved upon awakening. Overall, the recorded-data ratio exceeded 96%. After excluding > 100 μV chewing artefacts or abrupt

interface disturbances, the valid-data ratio remained above 88% **(Fig. 5f and Methods)**. These results establish week-scale, real-time brain recording and brain-behavior mapping with an earhook wireless EEG system. It also shows that the attention index captures interpretable, task-specific spectral-spatial signatures that generalize across days and contexts.

Discussion

We present a fully breathable, hair-compatible, 16-channel wearable EEG system that enables continuous, week-scale brain recording with smartphone-based, real-time attention assessment in everyday settings. An in situ-gelled macroporous hydrogel coupled to a flexible Ag/AgCl mesh electrode establishes a stable hair-bearing scalp–hydrogel–electrode interface that resists drying, slipping on hair, and friction. Together with a lightweight earhook wireless module, macroporous Ecoflex encapsulation, and wireless charging during sleep, the system maintains comfort and uptime suitable for longitudinal use. These capabilities open avenues for continuous neurological disease tracking, learning and performance support, workplace safety, and basic neuroscience outside the lab.

Methods

Preparation of the macroporous hydrogel

A macroporous hydrogel was prepared by a one-pot foaming-gelation process. DA·HCl (0.4 g, Sigma-Aldrich) was dissolved in 4.0 mL deionized water at 75 °C. TA (0.3 g, Aladdin Industrial Corporation), glycerol (3.0 g, Aladdin Industrial Corporation), and gelatin (2.5 g, medium gel strength, Sigma-Aldrich) were then added sequentially with continuous high-speed magnetic stirring at the same temperature until fully dissolved. The mixture was stirred at 1,000 rpm for 2 h, during which vortex-induced turbulence entrained air into the solution and generated a uniform dispersion of bubbles that served as transient templates for macropore formation. The increased viscosity imparted by DA·HCl and TA suppressed bubble coalescence and rupture. The resulting bubbly precursor was subsequently cooled to room or physiological temperatures (33–35 °C) to induce gelatin gelation, thereby locking in the macroporous architecture. Formulation variants used for optimization are listed in **Supplementary Table 4**.

Fabrication of flexible Ag/AgCl mesh electrodes

Flexible Ag/AgCl mesh electrodes were fabricated by laser-cutting (UV-100 laser cutter, Han's Laser, China) a 20 μm-thick silver substrate into a circular mesh structure (diameter: 5.3 mm; mesh size: 0.25 mm × 0.25 mm). The silver substrate was supplied by Guangming Technology Research Materials Co., Ltd. A thin commercial conductive wire was soldered to the circular mesh as the electrical lead, and the resulting silver mesh was subsequently immersed in sodium hypochlorite solution (commercial "84" disinfectant, available chlorine content of 13.6−18.4 g L^{-1} according to the product label) at room temperature until the surface was fully converted to Ag/AgCl, as indicated by a uniform gray appearance. After chlorination, the electrodes were dried in a 60 °C oven and stored in a sealed container before use.

Fabrication of a flexible and breathable 16-channel earhook wireless module

The analog front end of the small earhook wireless module includes two ADS1298 chips (Texas Instruments, USA) and an R-C low-pass filter network, which provides simultaneous 16-channel EEG measurement with low noise, compact size, and low power consumption. The EEG signals are sampled at a rate of 250 Hz and sent to a BLE System on a Chip (SoC) (nRF52840, Nordic Semiconductor, Norway) on the module. Then the signals are further filtered and downsampled to 125 Hz to reduce communication overhead and optimize power consumption before being transmitted wirelessly via BLE to the computer or the smartphone. The module is powered by a small rechargeable Li-Poly battery with a capacity of 400 mAh. To achieve good noise performance, a low dropout (LDO) regulator (LP5907, Texas Instruments, USA) is applied to provide a low-noise 3.3 V power supply for the analog part. The overall current consumption of the module is about 6.4 mA. This gives around 2.6 days of continuous EEG signal monitoring with the small battery. To extend operation time, a wireless charging subsystem was integrated, consisting of a wireless power receiving coil, a wireless power receiver chip (NU1680, NuVolta Technologies, China), and a battery linear charger. Through a wireless power transmitter embedded in a pillow, wireless charging can be achieved while sleeping without disconnecting the device, thus enabling uninterrupted long-term EEG signal monitoring.

The circuit board is manufactured using a 4-layer polyimide (PI) flexible printed circuit board (fPCB). The design and production of the circuit were completed with the assistance of WeSys Technology Co., Ltd, China. The analog front end and BLE SoC are fabricated on one circuit board

in the earhook module, and the wireless charging system is made on a separate tiny circuit board together with the battery. The assembled wireless module measures 75 mm × 55 mm × 10 mm and weighs 24.5 g. After assembling the wireless-module circuitry, we implemented a hierarchical encapsulation scheme to produce a flexible, breathable earhook module optimized for long-term conformal wear at the bioelectronic interface. At the skin contact surface, a macroporous layer was fabricated via a sacrificial template approach: biocompatible Ecoflex 00-20 FAST silicone was cast with 0.3−0.6 mm sucrose particles as removable porogens, generating anisotropic through-thickness permeation channels after porogen removal. This porous layer enhanced water-vapor transport and gas exchange, whereas non-contact regions retained a continuous, non-porous encapsulation to preserve mechanical integrity and environmental sealing. The resulting anisotropic encapsulation reconciles epidermal breathability with sustained electronic reliability during multi-day wear. A green LED was used as a system-status indicator and flashed at a frequency of 0.5 Hz upon initiation of EEG recording.

Structural, morphological, and rheological characterization

FTIR spectra were acquired on a FTIR spectrometer (Nicolet iS50, Thermo Scientific, USA) in attenuated total reflectance (ATR) mode over 4,000−800 cm^{-1}, with 32 co-added scans at 4 cm^{-1} resolution. Macroporous hydrogel morphology was observed using a digital microscope (AM7515MT8A, Dino-Lite, Japan). Pore size distribution was quantified from optical images using ImageJ. For SEM, glycerol removal during freeze-drying led to pore collapse; therefore, samples (with and without macroporosity) were prepared without glycerol and dried at ambient conditions for 12 h to preserve the pore architecture. The dried samples were then fractured to expose cross-sections and imaged using a scanning electron microscope (TM4000, Hitachi, Japan) at an accelerating voltage of 15 kV. Gelation kinetics, thermoreversibility and self-healing property were evaluated on a rheometer (HR-1, TA Instruments, USA). Time-sweep oscillatory tests at 35 °C (parallel-plate geometry, 20 mm diameter, 1 mm gap, 1% strain) were used to determine the critical gelation time, defined by the crossover of the storage (G′) and loss (G″) moduli. Thermoreversibility was assessed by dynamic temperature sweeps during cooling (75 °C to 10 °C) and heating (10 °C to 75 °C) at 2 °C min^{-1} under 1% shear strain.

Mechanical and interfacial toughness characterization

Mechanical testing was performed on a universal testing machine (ESM303, Mark-10, USA). For tensile stress, rectangular hydrogel specimens (with an effective area of 5.0 mm × 5.0 mm× 0.2 mm) were clamped and stretched at 50 mm min^{-1} in a single cycle to obtain stress-strain curves. Fatigue resistance was evaluated by (i) single-cycle tests at 100−1,000% strain and (ii) 100 loading/unloading cycles at 300% strain under identical conditions. For compression, cylindrical hydrogel samples with an effective diameter area of 12 mm and a thickness of 2 mm were loaded at 13 mm min^{-1} using a 25 N load cell to obtain compressive stress–strain curves, followed by 500 cycles between 0% and 70% strain. Electrical resistance during compression was monitored in real time with an LCR meter (E4980AL, Keysight, USA) at a measurement frequency of 1 kHz and an oscillation voltage of 100 mV. To simulate interfacial shear during practical use, the 1 mm-thick hydrogel was mounted on an electrically driven reciprocating tribometer (ASR-S600, AISRY Instrument, China) and participated in cyclic reciprocating rubbing with a 7.2 mm-diameter polyurethane (PU) ball under a 50 g load at 40 cycles min^{-1}. Resistance changes were recorded simultaneously with a digital multimeter (DMM7510, Keithley, USA). Durability was assessed over 1,000 friction cycles. Interfacial toughness at hair-bearing skin–hydrogel and hydrogel–electrode interfaces was quantified by 90° peel tests. Hydrogels with dimensions of 15 mm × 10

mm × 10 mm were applied to smooth artificial skin or hair-bearing rabbit skin and peeled using a tensile tester (MTS E43.504, MTS Systems, USA; 50 mm min^{-1}, 50 kN load cell). Force–displacement data were recorded, and the interfacial toughness (peel energy) was calculated as the steady-state peel force divided by specimen width. The hydrogel–electrode interface was characterized using the same protocol.

Impedance profiling

Electrochemical impedance spectroscopy was performed on an electrochemical workstation (VersaSTAT 3F, Princeton Applied Research, USA) over 1 MHz−0.1 Hz. For intrinsic impedance, hydrogel specimens (1.0 cm × 2.0 cm × 0.2 cm) were placed on patterned interdigitated electrodes, and spectra were recorded in a two-electrode configuration. To approximate the interfacial contact impedance encountered during EEG acquisition, scalp contact impedance was measured using a three-electrode configuration: a hydrogel electrode with an applied thickness of approximately 1 mm and effective area of 0.78 cm^2 was placed on the hair-bearing scalp served as the working electrode, while hydrogel electrodes placed on the left and right ears served as the reference and counter electrodes, respectively. Before testing, the measured scalp site was gently cleaned with a mild exfoliating scrub, wiped with clean water, and the hair was parted to expose the scalp surface. Commercial EEG paste (Elefix V, Nihon Kohden, Japan) was applied at an adjacent site (~1.5 cm) as a control.

Experimental evaluation of hydrogel properties: porosity, gas permeance, WVTR, and anti-drying property

Conventional porosity measurements often rely on freeze-drying and ethanol immersion to infer pore volume from mass changes[44]. In our system, this requires prior glycerol removal by water exchange, which can collapse macropores and bias the result. To avoid solvent exchange, we quantified porosity by comparing the apparent density of a macroporous hydrogel to a composition-matched, non-porous reference, which was prepared from the same precursor after vacuum degassing before gelation. (i) Prepare paired cylindrical specimens (diameter 2.5 cm) of non-porous and macroporous hydrogels from the same batch. (ii) Measure thickness and compute volumes V_1 (non-porous) and V_2 (macroporous). (iii) Record masses m_1 (non-porous) and m_2 (macroporous). (iv) Calculate the porosity of the macroporous hydrogel using the following equation:

$$Porosity\ (\%) = (1 - \frac{m_2 * V_1}{m_1 * V_2}) \times 100 \quad (1)$$

Gas permeance tests were measured by a constant permeation volume method with a low-pressure membrane permeation system (HR-21, Gaorui, China) at a feed pressure of 0.5 bar and 25 °C. Gas permeance P_p (GPU) was calculated as[45]:

$$P_p = \frac{273}{76} \frac{V}{ATP_0} \frac{dP}{dt} \times 10^6 \quad (2)$$

Where V (cm^3) is the gas flux through the hydrogel, A (cm^2) is the effective sample area. T (K) is the experimental temperature. P_0 and P are the feed- and permeate-side pressures, respectively, and dP/dt ($cmHg^{-1}\ s^{-1}$) is the permeate side pressure rise rate. The hydrogel mass changed less than 0.5% before and after each run, indicating negligible dehydration.

To decouple water loss through the test hydrogel (1 mm-thick) from the hydrogel's intrinsic water exchange with the environment, we measured a reference (calibration) hydrogel with identical initial water content, thickness, and exposed area under identical conditions. Subtracting the mass

change of reference from that of the test specimen corrects for intrinsic exchange and yields the true water-vapor transmission. The corrected WVTR was calculated using the following equation.

$$WVTR = \frac{W_{mea} - W_{ref}}{A \times t} \quad (3)$$

Where W_{mea}, W_{ref}, A, and t are the water loss mass, the mass change of the reference sample, the bottle-opening area, and the test duration, respectively.

For anti-drying, the initial mass was weighed for all samples, which were then exposed in ambient conditions for 31 days. Mass was measured at 24 h intervals and calculated using the following equation.

$$Weight\ retention(\%) = \frac{m_t}{m_0} \times 100 \quad (4)$$

Where m_0 and m_t are the weight of the hydrogel at Day 0 and Day t, respectively.

Skin biocompatibility assessment

To evaluate the potential for negative skin response and sensation, a rigorous controlled patch-test study was conducted on 10 healthy adult volunteers (n = 10) following established dermatological protocols. Four 2 cm × 2 cm patches, (i) a commercial Ag/AgCl electrode, (ii) PDMS, (iii) 3M surgical tape, and (iv) the developed hydrogel (thickness of 1 mm), were applied to randomized, non-overlapping sites on the forearm for 24 h continuous contact (with 1 participant wearing the patches for 8 consecutive days to assess long-term compatibility). Before application, the skin was gently cleaned with alcohol. Patch locations were randomized across participants, and adjacent sites were separated by at least 1.5 cm to avoid overlapping or cross-interference. Upon patch removal, standardized photographs were taken, and participants performed a VAS self-assessment of local discomfort (0 = no discomfort, 10 = extreme). A board-certified dermatologist, blinded to material identity, subsequently graded the skin reaction at each site according to the ICDRG criteria (negative = "–"; doubtful positive = "+?"). This dual assessment provided both subjective and objective evidence of the materials' biocompatibility profiles.

Sleep signal acquisition and data processing

To benchmark our wearable wireless system against PSG standards, we conducted an overnight 8.5 h continuous sleep study in a healthy 33-year-old male participant in collaboration with the Sleep Medicine Department of Shantou University Medical College. Because the device is designed for EEG acquisition, analyses focused on EEG signals; auxiliary channels used for sleep staging (electrooculogram, electromyogram, electrocardiogram) were obtained from the PSG system. For side-by-side comparison, hydrogel electrodes, unless otherwise specified, were prepared with an applied thickness of approximately 1 mm and an effective contact area of about 0.78 cm^2, and were applied at F_3, F_4, C_3, C_4, O_1, and O_2 according to the international 10–20 electrode placement system, and commercial EEG paste electrodes were placed at adjacent sites (~1.5 cm). For wireless EEG acquisition, two additional hydrogel electrodes affixed to the ears (A_1, A_2) served as reference and ground electrodes, respectively. In all subsequent experiments, EEG data were acquired using the wireless system with the same electrode configuration as described above. The PSG served as the reference standard and included EEG recorded with commercial paste electrodes, as well as auxiliary channels for sleep staging: bilateral electrooculogram (EOG), submental electromyogram (EMG), electrocardiogram (ECG), nasal/oral airflow, thoracoabdominal respiratory effort belts, snore microphone, peripheral oxygen

saturation (SpO_2) with pulse, body position and actigraphy/movement sensors. During overnight sleep, EEG signals were continuously and simultaneously acquired using the standard PSG and wireless systems.

The EEG signals were band-pass filtered (1−35 Hz, finite impulse response (FIR)) and processed offline in MATLAB. The PSG and wireless EEG systems were originally sampled at 512 Hz and 250 Hz, respectively. PSG data were resampled to 250 Hz using MNE-Python to establish a common temporal resolution. The two systems were first aligned using recorded Beijing time stamps and then fine-synchronized within each 30 s sleep epoch using zero-mean normalized cross-correlation between paired channels. The lag search was restricted to ± 20 samples (± 80 ms at 250 Hz), and only temporally overlapping, valid segments were retained for subsequent analysis. For time-frequency analysis, the six recorded EEG channels in each system were averaged in the time domain after synchronization, and STFT was then applied separately to the PSG-averaged signal and the wireless-averaged signal using 4 s windows with 50% overlap and a Hann window. The resulting spectrograms were converted to decibel units and used to assess the consistency of spectral dynamics between the two systems. For sleep staging, the synchronized 8.5 h dataset from both systems was segmented into 30 s epochs, exported separately, and de-identified to conceal device identity. A certified sleep technologist scored the datasets blindly following AASM criteria (Wake, N1, N2, N3, REM). Agreement between the two hypnograms was quantified in MATLAB, including calculation of Cohen's kappa coefficient.

Motion artefact evaluation

A triaxial accelerometer was integrated into the earhook wireless module to quantify motion-induced artefacts and their impact on EEG fidelity. Hydrogel electrodes were applied at T_8, P_4, and F_4, with commercial EEG paste electrodes placed at adjacent sites (~1.5 cm) as controls. To enable a direct comparison of interfacial performance, both conditions used the same mesh Ag/AgCl electrode and identical lead connections; only the conductive coupling medium was changed from hydrogel to commercial EEG paste. For treadmill-based motion-artefact assessment, the participant (25-year-old healthy male) performed slow walking (2.0 km h^{-1}), fast walking (5.0 km h^{-1}), and running (6.5 km h^{-1}). EEG signals and acceleration were co-recorded for over 2 min per condition.

The EEG signals were band-pass filtered (1−35 Hz, FIR) and processed offline in MATLAB. Acceleration signals were recorded simultaneously along three orthogonal axes corresponding to the anterior–posterior (Ax), medial–lateral (Ay), and vertical (Az) directions. Before frequency-domain analysis, the acceleration signals were corrected to remove the static gravitational component. Because gait-related impacts were most prominent along the vertical axis, subsequent frequency-domain and time-frequency coupling analyses focused on Az as the primary reference signal. FFT spectra of the EEG and Az signals were computed to identify gait-related spectral components. Spectral power at the step frequency and its harmonics was used to quantify speed-dependent coupling between motion and EEG. Time-frequency coupling between EEG and Az was further evaluated by wavelet coherence analysis. Relative phase between the two signals was extracted from the complex wavelet cross-spectrum.

For visualization and artefact identification, coherence values below 0.75 were excluded, and components with coherence > 0.75 at the step frequency or its harmonics were classified as motion-locked artefacts[46,47]. In the treadmill experiments, the analysis was limited to step-frequency-locked components referenced to the simultaneously recorded acceleration signals and

did not attempt to capture all non–gait-locked sources of contamination. For SNR quantification, EEG PSD was estimated for each speed using Welch's method. The step frequency for each condition was determined from the dominant peak in the vertical acceleration (A_Z) spectrum. Motion-related noise power was defined as the integrated EEG spectral power within frequency intervals centred at the step frequency and its harmonics up to the sixth order, within the 1.5–30 Hz band. Motion-related noise power (P_{noise}) was defined as the integrated EEG spectral power within frequency intervals centred at the step frequency and harmonics 2–6. Signal power (P_{signal}) was defined as the residual EEG power within 1.5–30 Hz after exclusion of these motion-related spectral components. SNR was then calculated as follows:

$$SNR_{dB} = 10\log_{10}\left(\frac{P_{signal}}{P_{noise}}\right) \quad (5)$$

Where P_{signal} and P_{noise} denote the signal power and noise power, respectively.

EEG monitoring under sweat condition

To further assess interfacial robustness under high-sweat conditions, an additional pre- and post-exercise experiment was performed using the same three channels (T_8, P_4, and F_4) and the same hydrogel-versus-commercial EEG paste configuration. EEG was recorded under the same treadmill condition (2.0 km h^{-1}) before exercise and again immediately after 45 min of vigorous exercise intended to induce substantial perspiration. The electrode positions, recording configuration, and acquisition parameters were kept unchanged between measurements. EEG signals and SNR values were then compared before and after exercise to determine whether signal fidelity and motion robustness were preserved under perspiration-conditioned interfacial stress. A healthy 25-year-old male participated in this experiment.

Comparison of continuous 24 h daily EEG monitoring, hydrogel versus commercial EEG paste electrodes

To evaluate long-term performance under daily-life conditions, a continuous 24 h EEG was recorded using the wireless system in a 25-year-old male participant. A hydrogel electrode was placed on the occipital scalp (O_2 channel) according to the international 10–20 system, and a control electrode prepared with commercial EEG paste was positioned at an adjacent site (~1.5 cm). A triaxial accelerometer integrated into the wireless module was used to record motion simultaneously. The participant maintained routine daily activities throughout the recording period and intermittently performed four treadmill walking sessions at 5.0 km h^{-1} to introduce controlled motion perturbations. The participant logged in real time the onset times of representative daily activities, including eating, sleeping, deskwork, smartphone, and other daily routines, as well as the onset of the four treadmill sessions. These activity annotations were associated to a temporal uncertainty of 1–5 s.

EEG data were first band-pass filtered offline (1–35 Hz, FIR), followed by a conservative artefact rejection procedure. Whenever the absolute EEG amplitude exceeded ± 100 μV, a 4 s window centred on the threshold-crossing event was discarded. This threshold served as a conservative criterion for excluding segments with large-amplitude non-neural contamination, such as chewing, gross ocular activity, facial muscle activity or abrupt interface disturbances. STFT spectrograms were computed using the same parameters as in the sleep experiment. FFT-based spectral estimates were generated with the same settings as in the motion artefact analysis to assess the correlation between Az and EEG signals across matched time windows.

EEG data processing and development of a smartphone-based LSTM model for real-time attention assessment

Hydrogel electrodes were placed at the standard 10–20 system, frontal (F_3, F_Z, F_4), central (C_3, C_Z, C_4), parietal (P_3, P_Z, P_4, P_7, P_8), occipital (O_1, O_Z, O_2), and temporal (T_7, T_8), to acquire 16-channel EEG signals. EEG signals were acquired using the wireless system during three behavioral states: (i) a high-attention Schulte Grid number-search cognitive activity trials and (ii) a low-attention condition of 3 min relaxing activities and (iii) sleep. For each Schulte Grid trial, the task completion time (t) was recorded.

The EEG signals were processed with the same band-pass filter as before (1–35 Hz; FIR). Whenever the absolute EEG amplitude exceeded ± 100 μV, a 4 s window centred on the threshold-crossing event was discarded. After preprocessing, PSD was computed with Welch's method (Hann window, 50% overlap; density scaling) in MATLAB. Segment periodograms were averaged across 16 channels to obtain the PSD, which was plotted over 4–30 Hz.

Scalp topography and functional connectivity were analyzed and visualized using MNE-Python. For scalp topography analysis, EEG data from the corresponding time periods under different activity states were selected, and the power spectrum of each channel was calculated. Band-limited power was then extracted separately in the θ-, α-, and β-bands, and the resulting channel-wise dB power distributions were projected onto the scalp to generate topographic maps of EEG activity.

Functional connectivity was quantified as pairwise spectral coherence between all EEG channel pairs. Continuous EEG data were segmented into fixed-length 2 s epochs, and coherence was estimated using multitaper spectral estimation. Connectivity was computed separately in the θ-, α- and β-bands, and organized as channel-by-channel connectivity matrices for each condition. For visualization, circular graphs were generated by displaying only channel pairs with connectivity values greater than 0.9, in order to highlight the strongest network connections under different activity states.

For model development, the dataset comprised three healthy participants (two males aged 23 and 28 years, and one female aged 26 years). Each participant underwent approximately 2 h of alternating high-attention (Schulte Grid task) and relaxation conditions. In addition, nocturnal EEG recordings were collected from the same participants during natural sleep, and corresponding segments were included to represent a low-attention state.

To prevent information leakage arising from the high overlap between adjacent segments, dataset partitioning was first performed at the trial level. Specifically, for each participant, trials were divided chronologically, with the first 70% assigned to the training set and the remaining 30% used for validation. Each trial corresponded to either a high-attention (Schulte Grid task) or relaxation condition and was labeled accordingly. This ensured that all data derived from a given trial were exclusively assigned to a single set.

In addition, the dataset also included EEG segments acquired during nocturnal sleep from the same participants. The overall dataset was approximately balanced across the three conditions (high-attention, relaxation, and sleep), with a ratio close to 1:1:1.

EEG signals within each trial were then transformed into time–frequency representations using a STFT with a 2 s window and 50% overlap. Spectral features within the 4–30 Hz frequency band were extracted and assembled into 20 s analysis segments. Consecutive segments were generated with a step size of 1 s. For each segment, channel-wise spectral features were reshaped into a two-

dimensional feature matrix and used as the input to a recurrent regression model. The model architecture consisted of three LSTM layers for temporal feature extraction, followed by a fully connected layer and a bounded linear activation function defined as min(max (0, x), 1), implemented as Hardtanh (0, 1), to constrain the output within the target range. Attention scores were defined within the range of 0–100 and were linearly normalized to 0–1 during training. The model outputs were subsequently rescaled to the 0–100 range for evaluation and interpretation. Scores were updated once per second, with each estimate reflecting the preceding 20 s of data.

Supervision labels were assigned based on experimental conditions and task performance. For the high-attention Schulte Grid condition, all 20 s EEG segments derived from a given trial were assigned the same attention label according to the trial completion time. Among the remaining trials, the shortest completion time was assigned a label of 100 and the longest a label of 85, with intermediate trials linearly mapped between these bounds. Thus, shorter completion times corresponded to higher attention scores. EEG segments acquired during the relaxation condition were assigned a label of 20, and sleep segments were assigned a label of 0. In total, 26,548 labeled 20 s segments were obtained, of which 18,730 were used for training and 7,818 for internal validation.

Generalization was evaluated in 6 healthy participants (2 males aged 25 and 26 years, and 4 females aged 24, 27, 27, and 28 years). Each participant completed a focused number-search task, a distraction condition and an eyes-closed relaxing condition. In the distraction condition, attentional load was reduced by conversation with another person. The focused and distracted conditions each lasted approximately 3 min, and an approximately 3-min eyes-closed relaxing period was inserted between tasks as a low-cognitive-load control. EEG was recorded continuously throughout the experiment, and the smartphone model generated attention scores in real time.

After each condition, participants rated their perceived attention for the corresponding period on a 0–100 numeric scale, with higher values indicating greater perceived attention. Model-predicted attention scores were then compared with these self-reported ratings.

To further evaluate model performance in a practical application scenario, an additional simulated driving experiment was conducted in one 24-year-old female participant. The participant sequentially completed four experimental conditions: focused driving, relaxation, re-focused driving after rest, and distracted driving induced by a phone call. EEG data were recorded simultaneously under each condition, and model-derived attention scores were computed to assess the sensitivity of the model to dynamic changes in attention.

Eight-day continuous daily EEG monitoring and data processing

To validate the long-term operational stability and data usability of the wireless system under real-world conditions, a 30-year-old healthy male underwent 8 consecutive days of free-living EEG monitoring with real-time attention assessment. The electrode layout, recording hardware, and analysis pipeline were identical to those used in the real-time attention experiment. EEG signals were acquired at 250 Hz using the same reference and ground configuration described above. During the 8-day recording period, the device and electrodes remained continuously worn without removal, replacement, or repositioning. The participant was allowed to continue normal activities, including showering, sleeping, deskwork, eating, walking, exercise, and other routine behaviors. The battery supported approximately 2.6 days of operation when fully charged. To maintain uninterrupted long-term recording, the device was intentionally recharged wirelessly during sleep or daytime naps. The participant recorded all daily activities and their start times in real time.

These activity times corresponded to the timestamps of the EEG signals and attention scores recorded by the smartphone. The temporal uncertainty of manual activity logging was estimated to be approximately 1–5 s.

The EEG signal data were processed using the same method as above. Daily ridge plots of attention level were generated in MATLAB by binning the attention scores into 20 intervals and normalizing the histogram counts to relative counts for each activity and day. The highest point of each distribution, defined as the histogram mode of attention level (referred to as "mode" in the main text), represents the most frequent attention state within that activity and was annotated in each ridge plot. Scalp topographies and engagement index were processed using the same procedure as in the previous experiment. The engagement index was defined as the β-band ratio divided by the sum of the θ- and α-band fractions, i.e., $\beta/(\theta + \alpha)$. Band fractions were computed from the 16-channel average PSD and normalized to total power over 1–30 Hz. Ratios were defined as band-limited power divided by total band power, computed from the 16-channel average power. Total power was defined over 1–30 Hz to exclude direct current/baseline drift (< 1 Hz) and γ activity (> 30 Hz).

The time-frequency analysis followed the same preprocessing procedures described above. Notably, during the night of day 3, the participant scratched the scalp, which led to a fracture in the thin commercial wire of F_3 electrode and caused a disconnect. This resulted in approximately 10 h of lost signal. In the morning, we re-welded the wire to restore signal acquisition for the F_3 electrode. To preserve continuity in the sleep-stage time-frequency analysis, the F_3 signal was approximated only for the sleep analysis on day 3 as the average of the neighboring F_z and C_3 channels; no interpolation was applied in other time periods or analyses.

To quantitatively evaluate the completeness and usability of the EEG data during 8-day continuous monitoring, daily record ratio and valid-data ratio were further calculated. The record ratio was defined as the duration of EEG data successfully recorded on a given day divided by 24 h. The valid-data ratio was defined as the duration of artefact-free EEG data retained after artefact rejection divided by the duration of EEG data recorded on that day. The former was used to characterize recording completeness, whereas the latter reflected the proportion of recorded data that remained available for subsequent analysis.

On human experiments

The protocol for data acquisition was reviewed and approved by the institutional ethics committee (approval No. E20240902001). Written informed consent was obtained from all participants before enrollment. All participants had normal or corrected-to-normal visual and auditory acuity and no history of neurological disease or injury.

Data availability: All data supporting the findings of this study are available within this article and Supplementary Information or from the corresponding author upon request. Source data are provided with this paper.

References

1 Antonenko, P. *et al.* Using electroencephalography to measure cognitive load. *Educ. Psychol. Rev.* **22**, 425–438 (2010).

2 Gevins, A. *et al.* Monitoring working memory load during computer-based tasks with EEG pattern recognition methods. *Hum. Factors* **40**, 79–91 (1998).

3 Claassen, J. *et al.* Detection of electrographic seizures with continuous EEG monitoring in critically ill patients. *Neurology* **62**, 1743–1748 (2004).

4 Antony, A. R. *et al.* Systematic review of EEG findings in 617 patients diagnosed with COVID-19. *Seizure* **83**, 234–241 (2020).

5 He, Y. *et al.* Brain–machine interfaces for controlling lower-limb powered robotic systems. *J. Neural Eng.* **15**, 021004 (2018).

6 Ferreira, A. *et al.* Human-machine interfaces based on EMG and EEG applied to robotic systems. *J. Neuroeng. Rehabil.* **5**, 10 (2008).

7 Tatum IV, W. O. Long-term EEG monitoring: a clinical approach to electrophysiology. *J. Clin. Neurophysiol.* **18**, 442–455 (2001).

8 Biasiucci, A. *et al.* Electroencephalography. *Curr. Biol.* **29**, R80–R85 (2019).

9 Lin, C.-T. *et al.* Noninvasive neural prostheses using mobile and wireless EEG. *Proc. IEEE* **96**, 1167–1183 (2008).

10 Mullen, T. R. *et al.* Real-time neuroimaging and cognitive monitoring using wearable dry EEG. *IEEE Trans. Biomed. Eng.* **62**, 2553–2567 (2015).

11 Liao, L.-D. *et al.* Gaming control using a wearable and wireless EEG-based brain-computer interface device with novel dry foam-based sensors. *J. Neuroeng. Rehabil.* **9**, 5 (2012).

12 Mahmood, M. *et al.* Fully portable and wireless universal brain–machine interfaces enabled by flexible scalp electronics and deep learning algorithm. *Nat. Mach. Intell.* **1**, 412–422 (2019).

13 Xu, Y. *et al.* In-ear integrated sensor array for the continuous monitoring of brain activity and of lactate in sweat. *Nat. Biomed. Eng.* **7**, 1307–1320 (2023).

14 Ding, Y. *et al.* EEG-based brain-computer interface enables real-time robotic hand control at individual finger level. *Nat. Commun.* **16**, 5401 (2025).

15 Hsieh, J.-C. *et al.* Design of hydrogel-based wearable EEG electrodes for medical applications. *J. Mater. Chem. B* **10**, 7260–7280 (2022).

16 Im, C. *et al.* A review of electrodes for the electrical brain signal recording. *Biomed. Eng. Lett.* **6**, 104–112 (2016).

17 Shad, E. H. T. *et al.* Impedance and noise of passive and active dry EEG electrodes: a review. *IEEE Sens. J.* **20**, 14565–14577 (2020).

18 Chen, Y.-H. *et al.* Soft, comfortable polymer dry electrodes for high quality ECG and EEG recording. *Sensors* **14**, 23758–23780 (2014).

19 Li, G. *et al.* Towards real-life EEG applications: novel superporous hydrogel-based semi-dry EEG electrodes enabling automatically ‘charge–discharge’ electrolyte. *J. Neural Eng.* **18**, 046016 (2021).

20 Li, G.-L. *et al.* Review of semi-dry electrodes for EEG recording. *J. Neural Eng.* **17**, 051004 (2020).

21 de Vasconcelos, L. S. *et al.* On-scalp printing of personalized electroencephalography e-tattoos. *Cell Biomater.* **1**, 100004 (2025).

22 Patel, S. *et al.* Drawn-on-skin sensors from fully biocompatible inks toward high-quality electrophysiology. *Small* **18**, 2107099 (2022).

23 Wang, C. *et al.* On-skin paintable biogel for long-term high-fidelity electroencephalogram recording. *Sci. Adv.* **8**, eabo1396 (2022).

24 Yuk, H. *et al.* Hydrogel bioelectronics. *Chem. Soc. Rev.* **48**, 1642–1667 (2019).

25 Zhang, B. *et al.* A three-dimensional liquid diode for soft, integrated permeable electronics. *Nature* **628**, 84–92 (2024).

26 Kang, J. *et al.* Self-healing soft electronics. *Nat. Electron.* **2**, 144–150 (2019).

27 Lee, S. *et al.* Nanomesh pressure sensor for monitoring finger manipulation without sensory interference. *Science* **370**, 966–970 (2020).

28 Albulbul, A. Evaluating major electrode types for idle biological signal measurements for modern medical technology. *Bioengineering* **3**, 20 (2016).

29 Homan, R. W. *et al.* Cerebral location of international 10–20 system electrode placement. *Electroencephalogr. Clin. Neurophysiol.* **66**, 376–382 (1987).

30 Corbetta, M. *et al.* Control of goal-directed and stimulus-driven attention in the brain. *Nat. Rev. Neurosci.* **3**, 201–215 (2002).
31 Corbetta, M. *et al.* The reorienting system of the human brain: from environment to theory of mind. *Neuron* **58**, 306–324 (2008).
32 Berry, R. B. *et al.* The AASM manual for the scoring of sleep and associated events (American Academy of Sleep Medicine, Darien, IL, 2012).
33 Mantini, D. *et al.* Electrophysiological signatures of resting state networks in the human brain. *Proc. Natl. Acad. Sci. U.S.A.* **104**, 13170–13175 (2007).
34 Klimesch, W. EEG alpha and theta oscillations reflect cognitive and memory performance: a review and analysis. *Brain Res. Rev.* **29**, 169–195 (1999).
35 Engel, A. K. *et al.* Beta-band oscillations—signalling the status quo? *Curr. Opin. Neurobiol.* **20**, 156–165 (2010).
36 Cavanagh, J. F. *et al.* Frontal theta as a mechanism for cognitive control. *Trends Cogn. Sci.* **18**, 414–421 (2014).
37 Jap, B. T. *et al.* Using EEG spectral components to assess algorithms for detecting fatigue. *Expert Syst. Appl.* **36**, 2352–2359 (2009).
38 Pope, A. T. *et al.* Biocybernetic system evaluates indices of operator engagement in automated task. *Biol. Psychol.* **40**, 187–195 (1995).
39 Freeman, F. G. *et al.* Evaluation of an adaptive automation system using three EEG indices with a visual tracking task. *Biol. Psychol.* **50**, 61–76 (1999).
40 Lubar, J. F. Discourse on the development of EEG diagnostics and biofeedback for attention-deficit/hyperactivity disorders. *Biofeedback Self Regul.* **16**, 201–225 (1991).
41 Lubar, J. F. *et al.* Evaluation of the effectiveness of EEG neurofeedback training for ADHD in a clinical setting as measured by changes in TOVA scores, behavioral ratings, and WISC-R performance. *Biofeedback Self Regul.* **20**, 83–99 (1995).
42 Liu, D. *et al.* Interactive brain activity: review and progress on EEG-based hyperscanning in social interactions. *Front. Psychol.* **9**, 1862 (2018).
43 Ahn, S. *et al.* Interbrain phase synchronization during turn-taking verbal interaction—a hyperscanning study using simultaneous EEG/MEG. *Hum. Brain Mapp.* **39**, 171–188 (2018).
44 Cheng, J. *et al.* Fermentation-inspired gelatin hydrogels with a controllable supermacroporous structure and high ductility for wearable flexible sensors. *ACS Appl. Mater. Interfaces* **14**, 26338–26349 (2022).
45 Lei, L. *et al.* Carbon hollow fiber membranes for a molecular sieve with precise-cutoff ultramicropores for superior hydrogen separation. *Nat. Commun.* **12**, 268 (2021).
46 Nathan, K. *et al.* Negligible motion artifacts in scalp electroencephalography (EEG) during treadmill walking. *Front. Hum. Neurosci.* **9**, 708 (2016).
47 Grinsted, A. *et al.* Application of the cross wavelet transform and wavelet coherence to geophysical time series. *Nonlinear Processes Geophys.* **11**, 561–566 (2004).

Acknowledgements

The authors would like to thank Dr. Xiuli Hou from Department of Dermatology, Dezhou Hospital, Qilu Hospital of Shandong University for support with the skin biocompatibility evaluation in this work, Prof. Xuezhong He from Department of Chemical Engineering, Guangdong Technion-Israel Institute of Technology for support with the gas permeance evaluation, and Prof. Hossam Hacik from Department of Chemical Engineering, Technion-Israel Institute of Technology for his generous support of Yan Wang group's research at Guangdong Technion-Israel Institute of Technology.

Author contributions

Yan Wang conceived this concept. Zongman Zhang and Haoyang Wang developed the materials and performed the characterization experiments. Zongman Zhang, Haoyang Wang, and Shihong Lin designed the EEG and sustained attention assessments. Zongman Zhang, Haoyang Wang, Yi Liu, Wenqing Yan, Shihong Lin, Jiawei Yang, Zonglei Wang, Yuli Wang, Jiansheng Zhang, Yumiao Xu, Pengcheng Zhou, Yujie Zhang, Mingzhe Wang, Zichong Ji, Meiqiong Zheng, Shuaizhe Chen, and Yun Li performed the EEG-related experiments. Zongman Zhang, Haoyang Wang, Yi Liu, and Wenqing Yan performed all data processing and analysis. Tomoyuki Yokota and Sunghoon Lee contributed to discussing the data and results. Zongman Zhang, Takao Someya and Yan Wang analyzed the data and wrote the manuscript. Yan Wang and Takao Someya supervised the project. All authors discussed the results and commented on the manuscript.

Funding

The authors sincerely acknowledge the support from the National Natural Science Foundation of China (grant Nos.: 52303371, W2521021), Guangdong Science and Technology Department (grant Nos.: 2026A1515010704, STKJ2023075, 2021B0301030005), JSPS Bilateral Program (grant No.: JPJSBP120257419), the Japan Agency for Medical Research and Development (No.: JP223fa627001) and Japan Science and Technology Agency, CREST (No.: JPMJCR21P2), the Key Discipline (KD) Fund, Key Laboratory of Science and Engineering for Health and Medicine of Guangdong Higher Education Institutes, and the Start-Up Fund from Guangdong Technion-Israel Institute of Technology.

Competing interests

The authors declare no competing interests.

Fig. 1. Breathable wireless EEG system with macroporous hydrogel electrodes enabling 8-day continuous daily brain recording and attention assessment. a, (i) Photograph of an in situ-gelled macroporous hydrogel integrated with an Ag/AgCl mesh electrode in conformal contact with the hair-bearing scalp (top) and a magnified view of the hydrogel architecture (bottom). Scale bar, 2 mm (top); Scale bar, 500 μm (bottom). (ii) On-body demonstration of the earhook wireless EEG system. Scale bar, 1 cm. (iii) Photograph of the flexible and breathable 16-channel earhook wireless module connected to Ag/AgCl mesh electrodes via thin commercial wires (top) and exploded view of the earhook wireless module (bottom). Scale bar, 1 cm (top). Inset: magnified view of the Ag/AgCl mesh electrode. Scale bar, 10 μm. **b,** Attention-related cortical systems and scalp EEG coverage used in this study. (i) Schematic of cortical systems involved in attentional control, including frontal control-related processes, central-midline engagement and monitoring, parietal attentional orienting, occipital visual-attention modulation, and lateral temporal

reorienting or distributed network activity (left). Top-view of the 16-channel EEG montage spanning frontal (F_3, F_Z, F_4), central (C_3, C_Z, C_4), parietal (P_3, P_Z, P_4, P_7, P_8), occipital (O_1, O_Z, O_2) and temporal (T_7, T_8) sites. Dashed arrows denote broad correspondence between cortical systems and electrode groups (right). (ii) Smartphone-based real-time attention assessment: 16-channel EEG acquisition, transformation into time-frequency spectrograms via STFT, feature extraction using machine-learning algorithms, and on-device graphic display of attention level, dynamic attention curve, and 16-channel EEG signals. **c,** Eight-day continuous, real-time attention assessment during representative daily activities: (i) walking, (ii) casual smartphone use at a bus stop, (iii) deskwork, (iv) sleep. Scale bar, 10 cm. Inset in (i): minimal motion artefacts during walking. Insets of scalp topographies in (i–iv): β-band power each activity. Inset in (iv): wireless charging during sleep. Scale bar, 2 cm. Daytime, 06:00–18:00; nighttime, 18:00–06:00. The green LED flashed at a frequency of 0.5 Hz during EEG recording.

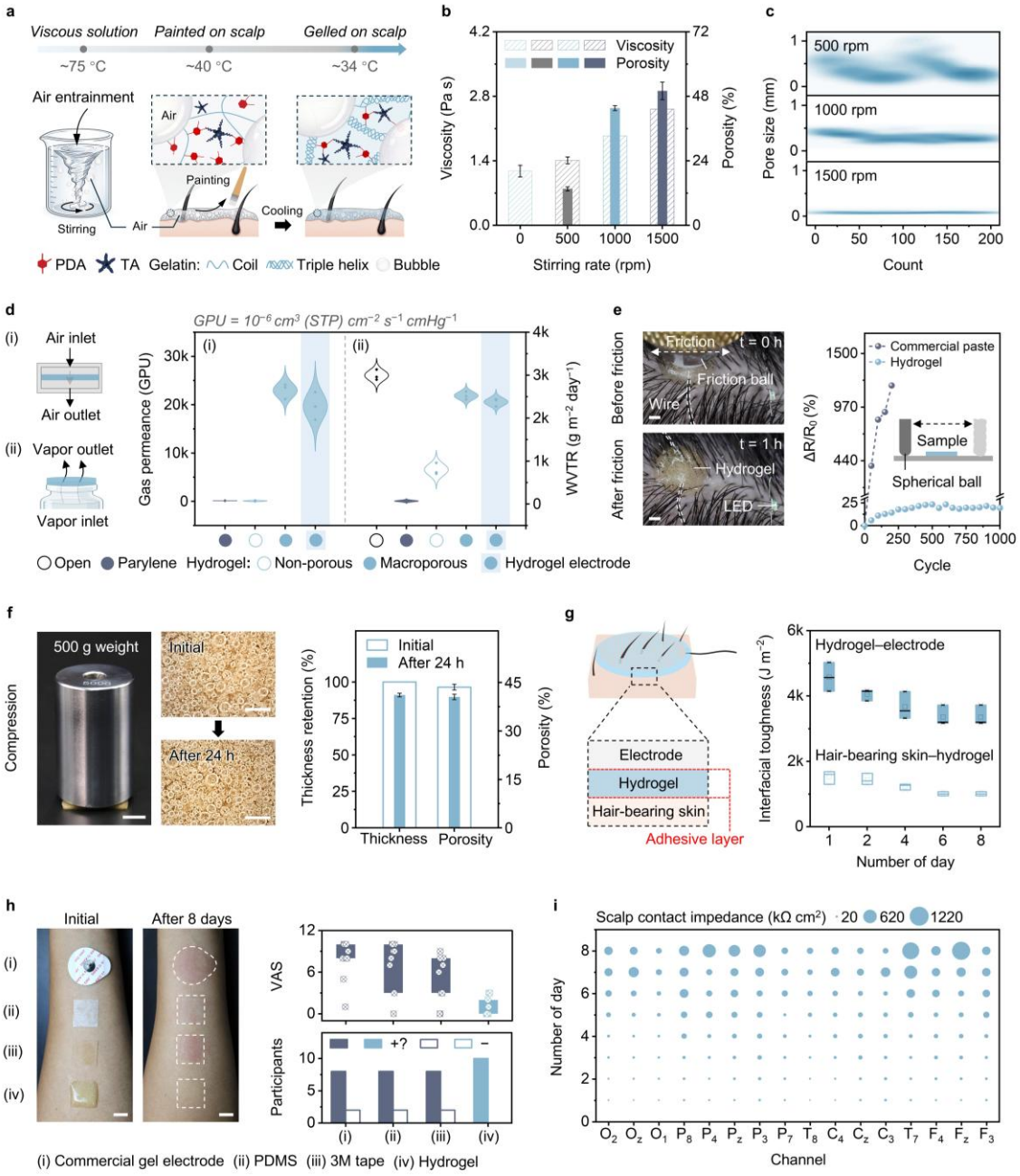

Fig. 2. Characterization of the macroporous hydrogel. a, Schematic of permeable scalp–hydrogel interface fabrication: air-bubble generation by stirring at ~75 °C, painting onto the hair-bearing scalp at ~40 °C, and cooling-induced gelation of the macroporous hydrogel. **b,** Dependence of viscosity and porosity on stirring speed. **c,** Pore-size distributions of the hydrogels. The x axis shows the number of counted pores, and the y axis shows pore size. **d,** Schematics (left) and measurements (right) of (i) gas permeance and (ii) WVTR. **e,** Photographs showing an LED remaining lit after 1 h of in situ friction on a hydrogel painted hair-bearing scalp (left) and electrical response during 1,000 friction cycles under a 50 g load for commercial EEG paste versus hydrogel (right inset, test setup). Scale bar, 20 mm. **f,** Photograph of the hydrogel compressed by a 500 g weight (left), optical micrographs before and after 24 h compression (middle), and changes in thickness and porosity (right; mean ± standard deviation (SD), n = 3). Scale bar (left), 1 cm; Scale

bar (middle), 1 mm. **g,** Schematic of the hair-bearing skin–hydrogel–electrode interface (left) and interfacial toughness at hydrogel–electrode and hair-bearing skin–hydrogel interfaces over 8 days (right). **h,** Skin biocompatibility initially and after 8 days for (i) commercial electrode, (ii) PDMS, (iii) 3M tape, and (iv) hydrogel (left), with visual analogue scale (VAS) (top right; "0" no discomfort, "10" extreme) and the International Contact Dermatitis Research Group (ICDRG) patch-test dermatitis scores (bottom right; '+?' doubtful positive, '–' negative). Scale bar, 1 cm. **i,** Eight-day monitoring of 16-channel scalp contact impedance.

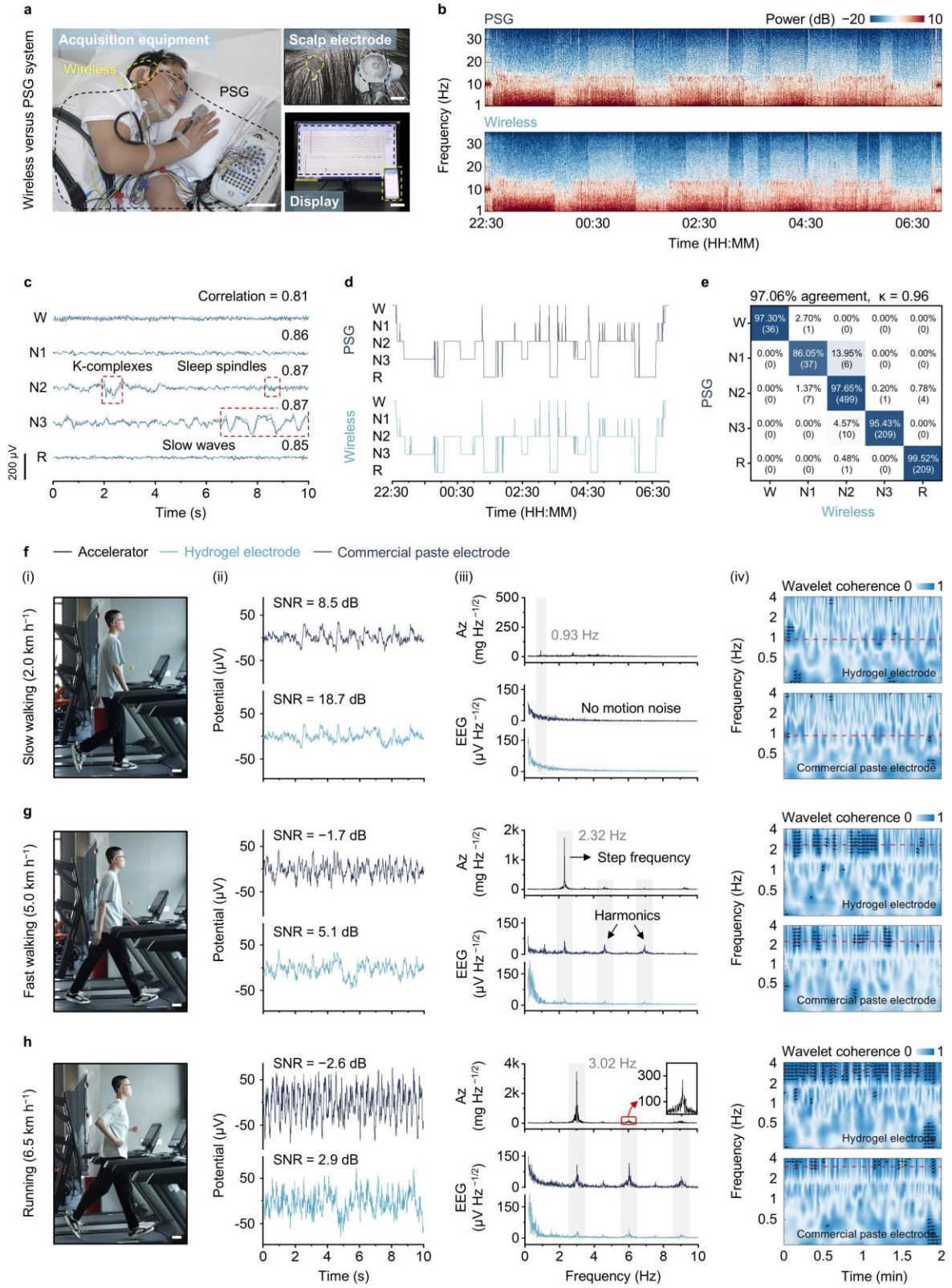

Fig. 3. PSG benchmarking and motion artefact evaluation. a, Photographs comparing acquisition hardware, scalp electrodes, and displays for PSG and the wireless system. Scale bar (left), 10 cm; Scale bar (top right), 5 mm; Scale bar (bottom right), 5 cm. **b,** Time-frequency

analysis using STFT recorded simultaneously by PSG and the wireless system over full 8.5 h sleep session. **c,** Representative 10 s EEG segments (F_4 channel) scored as W, N1, N2, N3, and R with PSG and wireless overlaid; dashed boxes highlight canonical features (K-complexes, spindles in N2, and slow waves in N3). Values at right indicate stage-specific Pearson correlation coefficients. **d,** Hypnograms from PSG and wireless across an 8.5 h recording; stages were scored in 30 s epochs by a registered sleep technologist. **e,** Confusion matrix heat map summarizing inter-system agreement for the epochs in (**d**). Cell values give the percentage of PSG-scored epochs assigned to each wireless stage; diagonal cells indicate per-stage agreement. Numbers in parentheses are counts of 30 s epochs. **f**–**h,** Motion artefact comparison at T_8 channel between commercial EEG paste and hydrogel electrodes during slow walking (2.0 km h^{-1}), fast walking (5.0 km h^{-1}), and running (6.5 km h^{-1}): (i) Photograph of each condition. Scale bar, 10 cm. (ii) Representative EEG signals and SNR. (iii) FFT amplitude spectra of Az and the corresponding EEG signals. (iv) Wavelet coherence between Az and EEG signals. The red dashed line marks step frequency: arrows denote relative phase (right, in-phase; left, anti-phase; upward, EEG lagging Az by 90°; downward, EEG leading by 90°). Coherence is shown only where > 0.75.

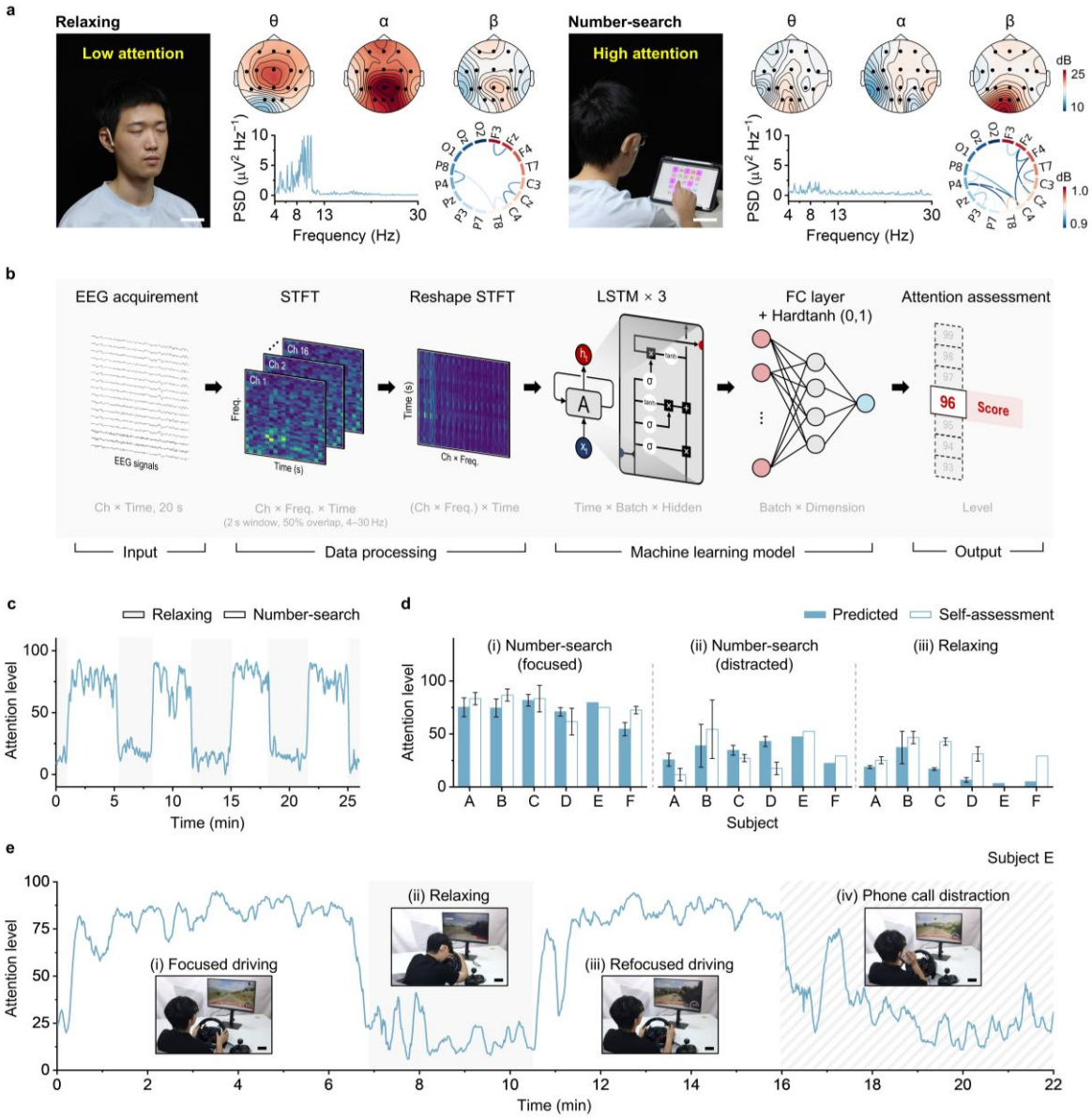

Fig. 4. Real-time attention assessment via smartphone-based machine-learning framework. **a,** Comparison of the relaxing state (low-attention) and the number-search task (high-attention) using photographs of the measurement scene, scalp topographies at θ-, α-, and β-band power (top), 16-channel averaged PSD (bottom left), and 16-channel EEG-based functional-connectivity networks (bottom right). Scale bar, 10 cm. **b,** Schematic of a machine-learning framework based on LSTM and fully connected layer for real-time attention assessment from 16-channel EEG signals. **c,** Real-time trajectories of attention level during an alternating number-search–relaxing–number-search paradigm. **d,** Comparison of model-predicted attention scores with Likert-scale self-assessed attention across 6 participants. **e,** Validation of the smartphone-based attention assessment system under 4 simulated driving conditions: focused driving, relaxing, post-rest focused driving, and distracted driving induced by a phone call; insets show representative photographs. Scale bar, 10 cm.

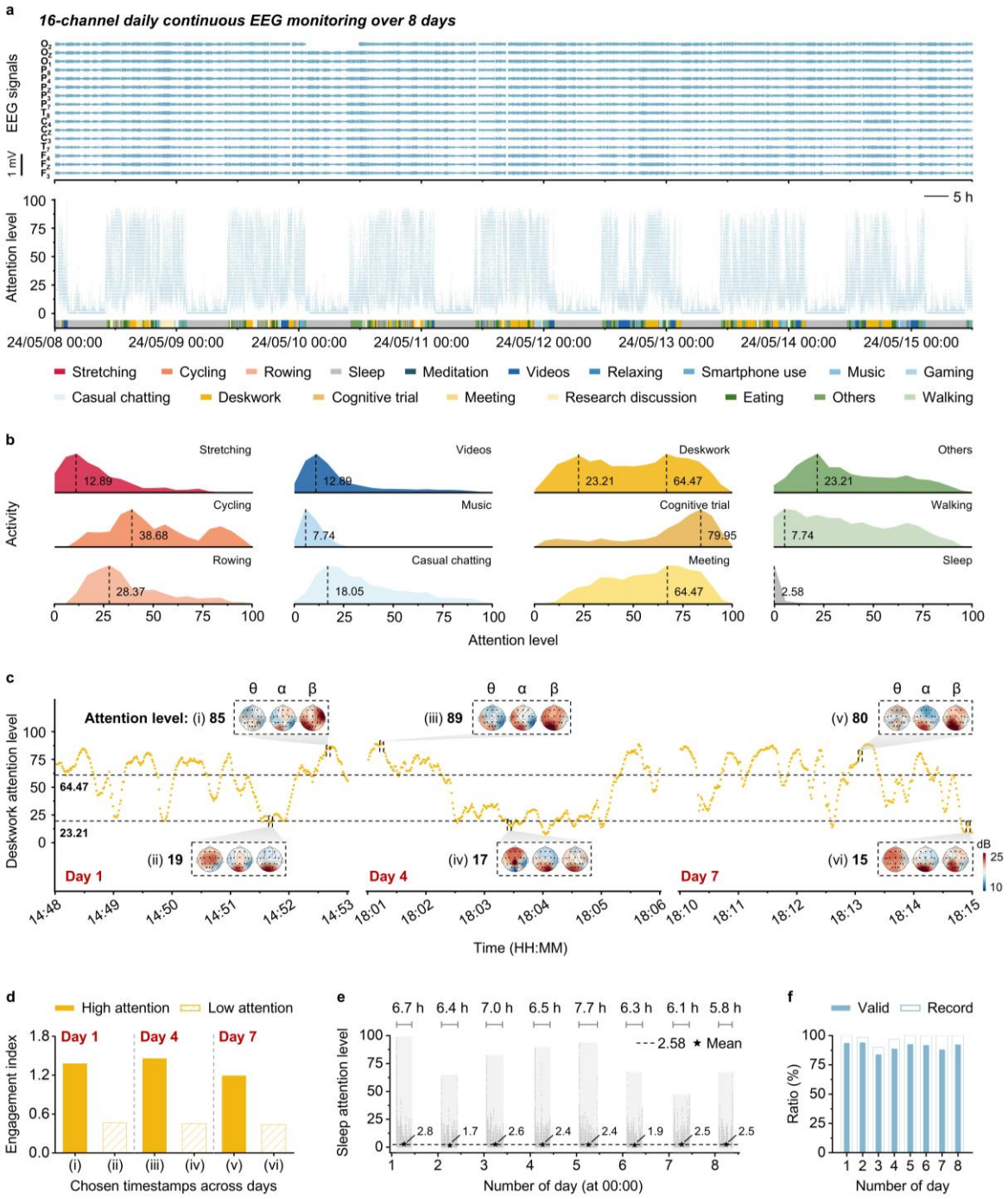

Fig. 5. Eight-day continuous daily EEG monitoring: real-time attention assessment and task-specific discriminability. a, Sixteen-channel EEG signals (top) and corresponding real-time attention level (bottom) over 8 consecutive days; activity annotations shown below. **b,** Ridgeline distributions of attention level for representative activities. X-axis: attention level (0–100); Y-axis: relative count. Dashed lines indicate the histogram mode of attention level, with the corresponding numeric values labeled. "Others" refers to activities such as washing dishes, using the toilet, and washing up. **c,** Attention trajectories during 3 representative 5 min deskwork sessions on Days 1, 4, and 7, with corresponding attention levels and scalp topographies of θ-, α-, and β-band power

shown for 6 selected moments (i–vi). **d,** Engagement index at high- and low-attention states for the 6 selected moments (i–vi). **e,** Attention levels across eight consecutive sleep sessions (Days 1–8). The dashed line marks the histogram mode of attention level from panel (**b**), the pentagram indicates the mean, and the width of the shaded rectangle represents hours of sleep. **f,** Ratio of valid data to total recorded data across the 8-day monitoring period.

Supplementary Files

This is a list of supplementary files associated with this preprint. Click to download.

- SI20260606.docx
- SupplementaryVideo1Robustadhesionatthehydrogelelectrodeinterface.mp4
- SupplementaryVideo2Demonstrationofhydrogelairpermeabilityinwaterandsoapywater.mp4
- SupplementaryVideo3ComparisonofsleepmonitoringusingthewirelesssystemandPSG.mp4
- SupplementaryVideo4RealtimewirelessEEGmonitoringandattentionlevelassessmentduringadrivingsimulation.mp4
- SupplementaryVideo5RealtimewirelessEEGmonitoringandattentionlevelassessmentduringdailyactivities.mp4
- SupplementaryVideo6Sleepmonitoringwithsimultaneouswirelessbatterycharging.mp4